RESEARCH ARTICLE | FEBRUARY 06 2025

Estimating depth-directional thermal conductivity profiles using neural network with dropout in frequency-domain thermoreflectance

Yasuaki Ikeda ; Yuki Akura ; Masaki Shimofuri ; Amit Banerjee ; Toshiyuki Tsuchiya ; Jun Hirotani

J. Appl. Phys. 137, 055106 (2025)
https://doi.org/10.1063/5.0248430
CHORUS

Journal of Applied Physics METHOD pubs.aip.org/aip/jap

Estimating depth-directional thermal conductivity profiles using neural network with dropout in frequency-domain thermoreflectance

Cite as: J. Appl. Phys. **137**, 055106 (2025); doi: 10.1063/5.0248430
Submitted: 12 November 2024 · Accepted: 20 January 2025 ·
Published Online: 6 February 2025

Yasuaki Ikeda, Yuki Akura, Masaki Shimofuri, Amit Banerjee, Toshiyuki Tsuchiya, and Jun Hirotani[a)]

AFFILIATIONS

Department of Micro Engineering, Graduate School of Engineering, Kyoto University, Kyotodaigaku-katsura, Nishikyo-ku, Kyoto 615-8540, Japan

[a)]**Author to whom correspondence should be addressed:** hirotani.jun.7v@kyoto-u.ac.jp

ABSTRACT

Non-contact and non-destructive methods are essential for accurately determining the thermophysical properties necessary for the optimal thermal design of semiconductor devices and for assessing the properties of materials with varying crystallinity across their thickness. Among these methods, frequency-domain thermoreflectance (FDTR) stands out as an effective technique for evaluating the thermal characteristics of nano/microscale specimens. FDTR varies the thermal penetration depth by modifying the heating frequency, enabling a detailed analysis of the thermophysical properties at different depths. This study introduces a machine learning approach that employs FDTR to examine the thermal conductivity profile along the depth of a specimen. A neural network model incorporating dropout techniques was adapted to estimate the posterior probability distribution of depth-wise thermal conductivity. Analytical databases for both uniform and non-uniform thermal conductivity profiles were generated, and the machine learning model was trained using these databases. The effectiveness of the predictive model was confirmed through assessments of both uniform and non-uniform thermal conductivity profiles, achieving a coefficient of determination between 0.96 and 0.99. For uniform thermal conductivity, the method attained mean absolute percentage errors of 1.362% for thermal conductivity and 3.466% for thermal boundary conductance (compared to actual values in the analytically calculated database). In cases of non-uniform thermal conductivity, the prediction accuracy decreased, particularly near the sample's surface, primarily due to the limited availability of machine learning data at higher heating frequencies.

I. INTRODUCTION

As semiconductor devices such as integrated circuits and power devices continue to undergo miniaturization, managing their increased heat generation density becomes a critical challenge.[1,2] These devices often feature complex structures and may incorporate materials with spatial variations in crystallinity, such as those produced through chemical vapor deposition[3–5] and ion-irradiation processes.[6] To enable optimal thermal design, precise mapping of the spatial distribution of thermophysical properties is essential. This task has garnered much attention, and various methods for measuring thermophysical properties have been developed, including thermoreflectance techniques,[4,7,8] scanning thermal microscopy (SThM),[9,10] Raman spectroscopy,[11,12] and lock-in thermography.[13] Notably, thermoreflectance methods, such as time-domain thermoreflectance (TDTR)[14–18] and frequency-domain thermoreflectance (FDTR),[19–22] have proven particularly effective for analyzing thermophysical properties and are extensively utilized in evaluating the properties of bulk materials,[19,23,24] thin films,[25,26] and multilayered structures.[27] In addition, they excel in capturing the thermal transport characteristics of samples with microstructural defects.[28–30] FDTR is especially favored owing to its straightforward measurement setup and its ability to adjust the depth of inspection by altering the laser heating frequency.

In FDTR, the sample absorbs the pump beam and is periodically heated by it. The temperature change alters the material's

reflectance, modulating the intensity of the reflected probe beam. This beam is then captured by a photodiode and processed through a lock-in amplifier synchronized with the pump beam's modulation signal to detect the phase lag between the two beams. A theoretical FDTR model[19] is applied to the collected data using the least-squares method to derive the thermophysical properties. Thermal conductivity is assessed by accounting for the structural and material characteristics of the sample. Additional technical details on the implementation of the FDTR method and thermal analysis can be found in previous studies.[31–33]

In this technique, the depth impacted by the measurement varies with the heating frequency, f, and can be estimated using the thermal penetration depth, d_p, defined as

$$d_p = \sqrt{\frac{k}{\pi C f}}, \tag{1}$$

where k and C represent the thermal conductivity and volumetric heat capacity of the sample, respectively. The analysis of thermal conductivity profiles in the depth direction can be enabled by controlling the heating frequency.[5,30] However, when examining the spatial profiles of complex structures, fitting parameters such as the thermal conductivity and heat capacity of the materials at different depths, as well as the thermal boundary conductance between different materials, need to be considered. Consequently, a substantial number of parameters must be determined using the least-squares method. However, using the least-squares method introduces dependencies and uncertainties in the fitting process. For example, if the initial settings are not accurate, the parameters may only be optimized locally, leading to unreliable results. To address these challenges, recent reports have explored the use of machine learning (ML) for FDTR measurements.[34–36] Shen *et al.*[34] developed a machine learning model to determine the initial values for the least-squares method, enhancing the stability of the fits. However, this machine learning model is restricted to specific, controlled parameters. Subsequently, Xiang *et al.*[36] proposed machine learning models that reconstruct depth-dependent thermal conductivity profiles from FDTR/TDTR measurements, even though their approach was limited to a linear combination of predefined functional forms. Due to multicollinearity and the constrained nature of these solutions, the accuracy of the predictions and the analysis of prediction uncertainty may be compromised. Therefore, it is crucial to address these issues by directly estimating the thermal conductivity values at each depth using a machine learning model with high expressivity and broad applicability.

While numerous machine learning algorithms are available, neural networks[37] stand out owing to their high expressivity, scalability, and broad applicability. Although the expressive power of neural networks makes them prone to overlearning, this issue can be avoided by employing the dropout method.[38,39] Moreover, using dropout with neural network models aligns mathematically with Bayesian approximation,[39] allowing for the estimation of the posterior distribution of thermophysical property predictions and thereby determining the prediction uncertainty.

In this study, machine learning models utilizing neural networks with dropout were developed to estimate the thermal conductivity profiles of samples. These models were designed to predict the thermal conductivity at each depth without imposing prior constraints on the profile's functional form. Calculations were conducted for scenarios where the thermal conductivity of the sample was uniform, as well as for cases where it varied with depth. The FDTR phase lag data, analytically generated for various thermal conductivity profiles and parameters, served as the training database. The effectiveness of the trained models was assessed using test sets derived from the training database. It was confirmed that the models can accurately estimate the posterior distribution of the thermal conductivity profile without prior limitations on the sample's thermophysical properties. In addition, the prediction uncertainty derived from the neural networks with dropout was found to be consistent with the physical interpretations.

II. METHODS

Figure 1(a) illustrates the sample configuration, which comprises two layers: a lower sample layer whose thermal conductivity varies with depth and an upper transducer layer. The development of a machine learning model for this system involves three stages: database creation, model training, and model evaluation.

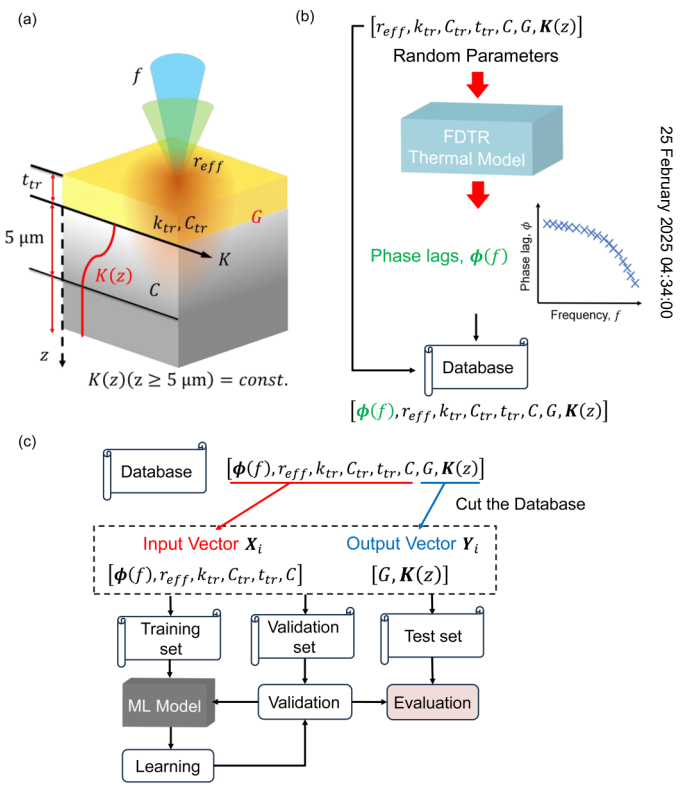

FIG. 1. (a) Frequency-domain thermoreflectance (FDTR) sample configuration. The system consists of two layers: the transducer and the sample. The sample's thermal conductivity varies with depth. (b) Process schematic for creating a training database to predict the depth-dependent thermal conductivity profile. (c) Process schematic for developing the machine learning (ML) model.

Initially, a database was constructed to represent the phase lag at each heating frequency in FDTR, as depicted in Fig. 1(b). The phase lags were calculated using several parameters, including the thermal conductivity k_{tr} and thickness t_{tr} of the transducer; the volumetric heat capacities C_{tr} and C of the transducer and sample layers, respectively; the depth-dependent thermal conductivity profile $\boldsymbol{K}(z)$; the thermal boundary conductance G between the sample and the transducer layer; and the effective $1/e^2$ beam spot radius r_{eff}. The laser heating frequencies were uniformly set across 400 points on a logarithmic scale ranging from 25 kHz to 200 MHz. It should be noted that measuring with FDTR at frequencies above 50 MHz presents challenges due to the low signal-to-noise ratio. However, considering the existence of an experimental system capable of operating at higher frequencies,[21,23] this frequency range was selected. To represent experimental noise, Gaussian noise with a standard deviation of 2% was added to the calculated phase lags. This procedure was repeated to compile the database.

In the second step of the process, the database was partitioned into input and output vectors to train the machine learning model, as depicted in Fig. 1(c). The outputs were the thermal conductivity profile of the sample and the thermal boundary conductance, while the inputs comprised the remaining parameters, such as the calculated phase lags. The database was further divided into training, validation, and test sets. The machine learning model was trained using the training set, with the validation set employed to monitor and evaluate the model's performance during training. The model that performed best on the validation set was then selected for final evaluation using the test set. For this study, the distribution of the database was as follows: 15% allocated to the test set, 12.75% to the validation set, and 72.25% to the training set.

The third step involved evaluating the trained machine learning model. The evaluation metrics used were the coefficient of determination R^2 and the mean absolute percentage error (MAPE) between the actual and predicted values. These are defined as

$$R^2 = 1 - \frac{\sum_{i=1}^{n} (h(\boldsymbol{X}_i) - \boldsymbol{Y}_i)^2}{\sum_{i=1}^{n} (\boldsymbol{Y}_i - \bar{\boldsymbol{Y}})^2}, \tag{2}$$

$$\mathrm{MAPE} = \frac{100}{n} \sum_{i=1}^{n} \left| \frac{h(\boldsymbol{X}_i) - \boldsymbol{Y}_i}{\boldsymbol{Y}_i} \right|, \tag{3}$$

where h represents the output from the machine learning model; $\boldsymbol{X}_i$ and $\boldsymbol{Y}_i$ $(1 \le i \le n)$ denote the ith input data and label data, respectively; and $\bar{\boldsymbol{Y}}$ is the average of the label data. Optimal conditions for the hyperparameters of the machine learning models were explored by conducting several training scenarios and evaluating the models using the metrics specified by Eqs. (2) and (3).

In the development of our machine learning models, the Monte Carlo dropout technique was implemented,[39] as illustrated in Fig. 2. This method involves temporarily deactivating some neurons in the hidden layers during the training phase, causing these neurons to output zero values to subsequent layers, irrespective of the input. This approach prevents overfitting by ensuring that the machine learning model does not overly depend on any single neuron. In addition, dropout was employed during the prediction phase to assess prediction uncertainty. By conducting multiple predictions with different sets of deactivated neurons, the posterior probability distribution of the predictions can be obtained.[39] In this study, 1000 repeated predictions were performed with dropout enabled. The mean of these 1000 predictions was taken as the predictive value, and the standard deviation was used to represent the prediction uncertainty.

To enhance the performance of the machine learning model, an exponential linear unit (ELU) function[40] was used for all activation functions within the neural networks. Although the rectified linear unit (ReLU) function[41–43] is widely utilized in contemporary neural networks, it is susceptible to issues such as the vanishing gradient problem[41,42] and the dead neuron phenomenon.[43] The ELU function defined below addresses these issues effectively and is known to improve performance,

$$f(x) = \begin{cases} x & (x > 0), \\ \alpha(\exp(x) - 1) & (x \le 0), \end{cases} \tag{4}$$

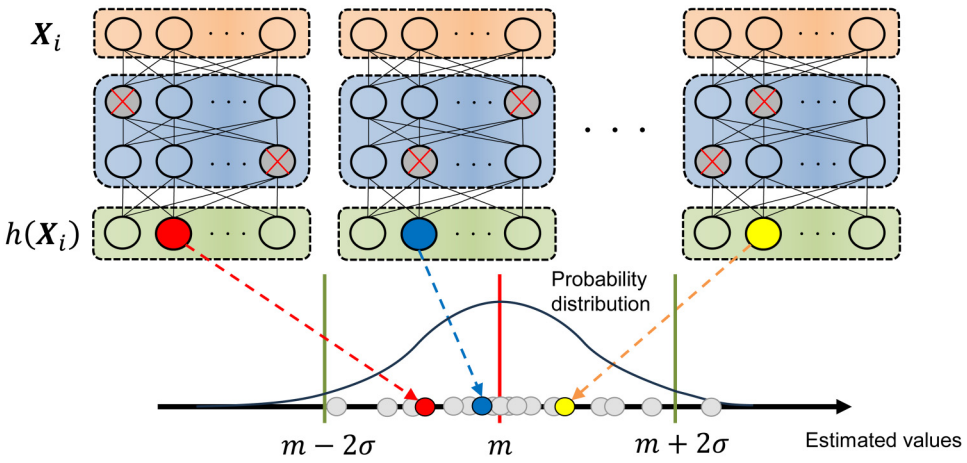

FIG. 2. Schematic illustration of the Monte Carlo dropout method. Each neuron is assigned a specific probability of yielding zero output. The distribution of outputs is generated by enabling dropout and iteratively recording the outputs. Here, m and σ represent the mean and standard deviation of the posterior probability distribution, respectively.

TABLE I. Error evaluation of predictions of thermal conductivity k_{sub} and thermal boundary conductance G for the model with uniform thermal conductivity.

	Evaluation	
Parameter	R^2	MAPE (%)
k_{sub}	0.9948	1.362
G	0.9620	3.466

where α is a hyperparameter, typically set to 1, which was also the case in this study.

The effectiveness of our machine learning models in analyzing FDTR data was assessed for samples exhibiting uniform thermal conductivity. Since the thermal conductivity was consistent across all depths, the thermal conductivity profile $\boldsymbol{K}(z)$ was simply a constant scalar value, k_{sub}. The parameter values were randomly selected within the ranges specified in Table S1 in the supplementary material, and the phase lags were subsequently calculated. It is important to note that these parameters were uniformly distributed on a logarithmic scale across different orders. The theoretical approach for computing phase lags in the FDTR model is detailed in Refs. 19 and 25.

Subsequently, a model for non-uniform thermal conductivity distributed across the sample depth was developed. In this model, thermal conductivity varied up to a depth of 5 μm, beyond which the layers were considered semi-infinite with constant thermal conductivity, as depicted in Fig. 1(a). The phase lags were computed by discretizing the thermal conductivity profile within the sample. The sample was segmented into N layers up to a depth of 5 μm, with each layer's thermal conductivity represented by the value at its center coordinates. The thermal boundary conductance between each discretized layer was assumed to be infinite, implying an absence of thermal resistance between layers. For this study, the discretization was set at $N = 500$, which ensures accurate calculation of the phase lags.[36] The detailed ranges of various parameters used in the database are provided in Table S2 in the supplementary material. The thermal conductivity profile $\boldsymbol{K}(z)$ was a vector—the output from the machine learning model—with 201 elements, corresponding to the thermal conductivities of the 200 layers from 0 to 5 μm and the constant thermal conductivity at depths beyond this. The method of constructing random thermal conductivity profiles is explained in the supplementary material, including Table S3 and Fig. S1.

For the case of uniform thermal conductivity, 400 000 datasets were generated using Python. Given that the predicted parameters span a broad range of magnitudes, it is essential to assess the accuracy of predictions using relative error. MAPE was employed as the error function for the machine learning model. The detailed architecture of the neural network used is illustrated in Fig. S2 in the supplementary material.

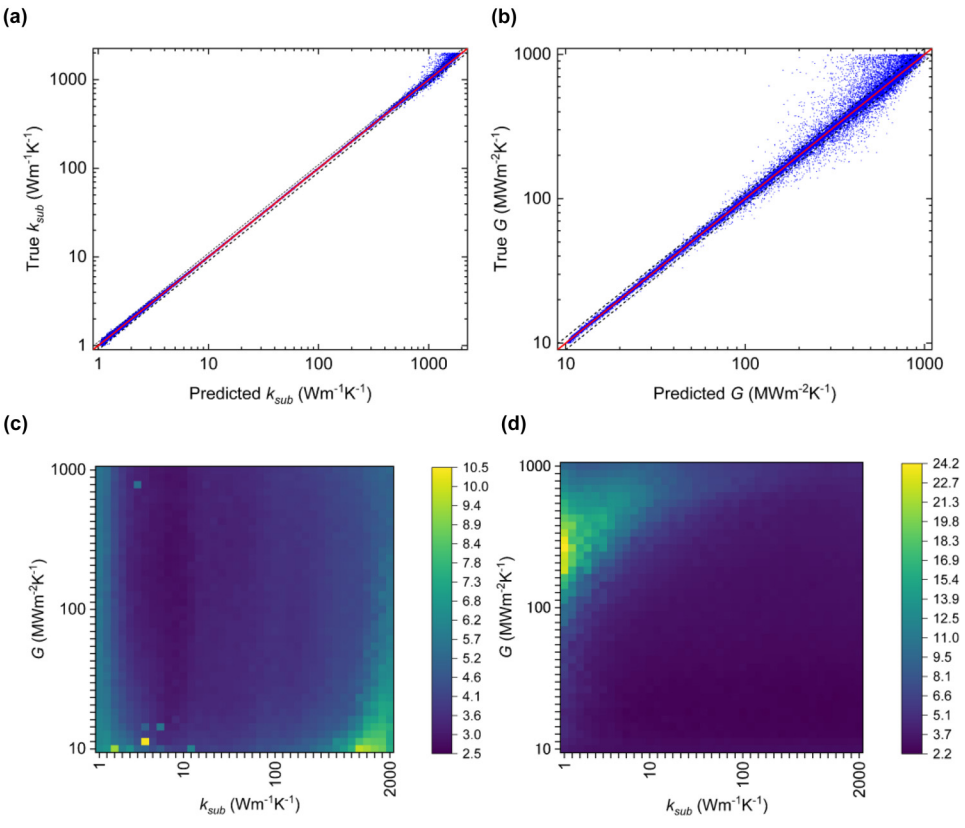

FIG. 3. Machine learning model predictions for uniform thermal conductivity model. (a) Sample thermal conductivity, k_{sub}. When data points are close to the solid red line, predictions are accurate. The black dashed lines indicate the ±10% prediction error interval. (b) Predictions for thermal boundary conductance, G. (c) Heatmap of prediction uncertainty using the Monte Carlo dropout method. The heatmap colors indicate the percentage of prediction uncertainty for k_{sub}. (d) Heatmap of prediction uncertainty for G.

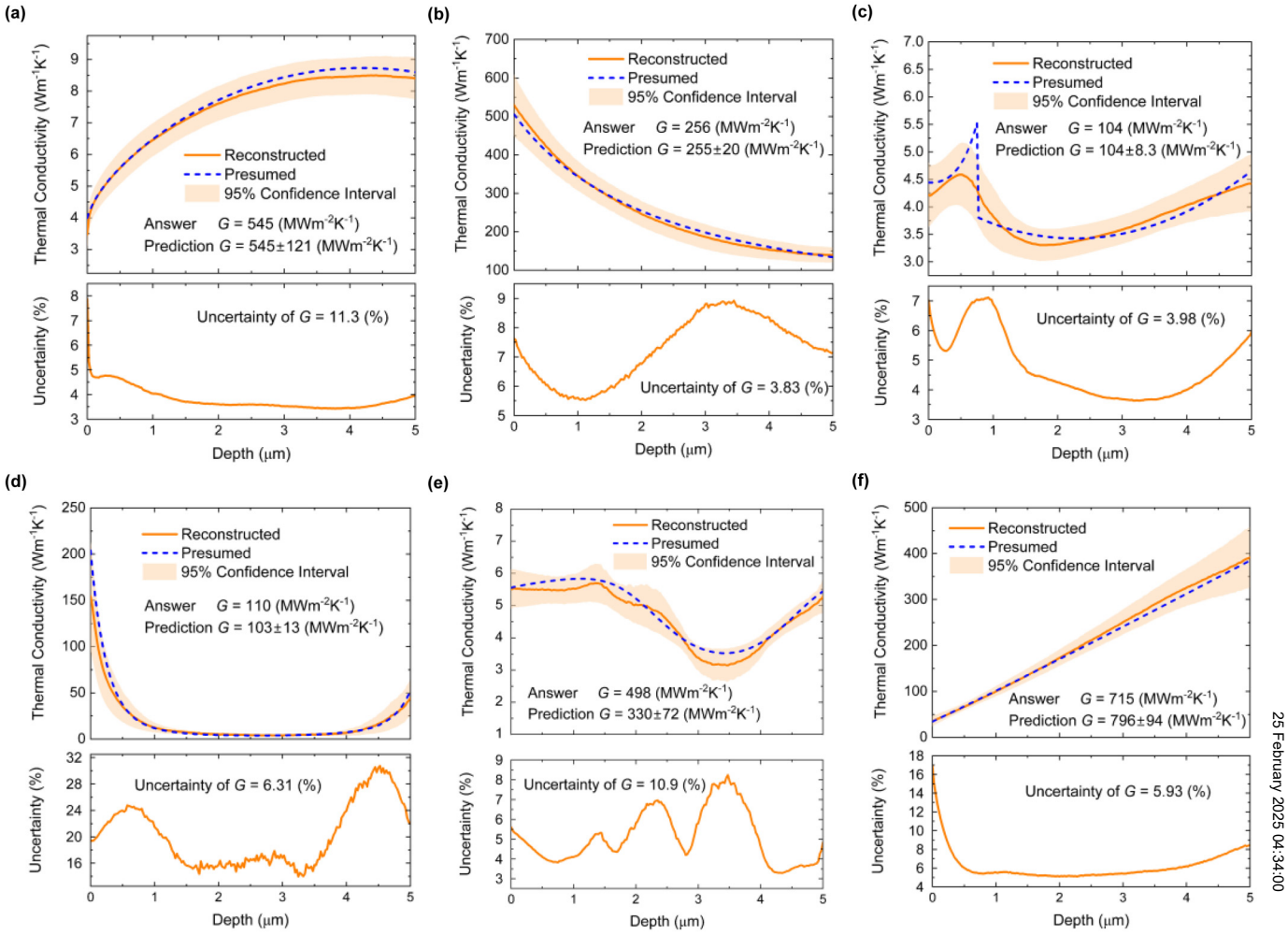

FIG. 4. (a)–(f) Examples of estimating depth-dependent thermal conductivity profiles for test sets. In each panel, the upper graph depicts the predicted thermal conductivity profile, while the lower graph shows prediction uncertainty as a function of depth. Orange areas denote 95% confidence intervals.

For the case of non-uniform thermal conductivity, a total of 500 000 datasets were generated. Because the machine learning model must predict a diverse array of profiles accurately, the root mean squared percentage error (RMSPE) was selected as the error function as follows:

$$\mathrm{RMSPE} = \sqrt{\frac{10\,000}{n}\sum_{i=1}^{n}\left(\frac{h(\boldsymbol{X}_i) - \boldsymbol{Y}_i}{\boldsymbol{Y}_i}\right)^2}. \tag{5}$$

The RMSPE is especially sensitive to outliers, making it suitable for ensuring the model can adapt to a broad range of profile variations. Detailed information regarding the neural network architecture and its hyperparameters is provided in Fig. S3 in the supplementary material.

III. RESULTS AND DISCUSSION

For the model with uniform thermal conductivity, Table I shows predictions of thermal conductivity and thermal boundary conductance for the test set using the trained neural network model. The MAPE values for thermal conductivity and thermal boundary conductance were 1.362% and 3.466%, respectively. Figures 3(a) and 3(b) plot the predicted values against the actual values. As depicted in Fig. 3(a), cases of extremely high or low thermal conductivity were noted, where the error margin occasionally exceeded 10%. Similarly, Fig. 3(b) shows that as the thermal boundary conductance increases, the error often surpasses 10%.

The influence of thermal conductivity and thermal boundary conductance on prediction uncertainty was investigated. Figures 3(c) and 3(d) display heatmaps that depict the uncertainties. The color gradients in the heatmaps correspond to the average prediction

uncertainties across different regions. As illustrated in Fig. 3(c), prediction uncertainty for thermal conductivity tended to increase in regions characterized by high thermal conductivity and low thermal boundary conductance. This trend can be attributed to the predominant influence of thermal boundary resistance on heat dissipation under these conditions. In addition, as shown in Figs. 3(a) and 3(c), there was an increase in both prediction error and uncertainty at extremely low thermal conductivities, primarily because heat dissipation in the transducer layer became more significant. Moreover, Figs. 3(b) and 3(d) illustrate that prediction errors and uncertainties for thermal boundary conductance escalated in areas with low thermal conductivity and high thermal boundary conductance; the restricted heat transfer to the sample lessened the impact of thermal boundary conductance on heat dissipation.

Figures 4(a)–4(f) present examples of predictions made using the trained neural network model for a system characterized by a non-uniform thermal conductivity profile along the depth. Additional examples of various functional forms and unsuccessful predictions are depicted in Figs. S4 and S5 in the supplementary material. The overall performance metrics for the thermal boundary conductance and thermal conductivity profile of the test set included an R^2 of 0.9904 and a MAPE of 4.013%. The MAPE values for predicted thermal conductivity at different depths are shown in Fig. 5(a), while Fig. 5(b) illustrates the average relative prediction uncertainty as a function of depth for cases of high and low thermal boundary conductance for the predictive distribution.

A higher thermal boundary conductance decreased the prediction uncertainty of the thermal conductivity profile but increased that associated with the thermal boundary conductance, and vice versa. These findings align with those for the model with uniform thermal conductivity, as shown in Figs. 3(a)–3(d). Moreover, Figs. 5(a) and 5(b) indicate that prediction errors and uncertainties tended to increase near the surface of the sample. This decrease in accuracy near the surface results from the restriction of thermal penetration depth by the upper-frequency modulation limit of 200 MHz, which complicates predictions of thermal conductivity in shallow regions. In addition, the MAPE reached a local maximum around a depth of 4 μm, as shown in Fig. 5(a), and prediction uncertainty increased as the depth approached 5 μm, as illustrated in Fig. 5(b). This may result from the boundary conditions of uniform thermal conductivity applied to regions deeper than 5 μm, as outlined in Fig. 1(a).

Notably, our database relies on analytical calculations. The analytical FDTR model may not fully replicate actual measurements because experimental datasets often capture phenomena that are not present in theoretical models. Consequently, incorporating experimental datasets into our training database would enhance the relevance and accuracy of our machine learning model. However, analytical methods allow for the generation of a diverse array of data types that are challenging to obtain experimentally, providing a large volume of data that enhances the learning efficiency and predictive accuracy of the model.

We also address the limitations of our method. As noted, the analytical FDTR model may not perfectly mirror actual measurements. For example, compared to our FDTR model illustrated in Fig. 1(a), more complex structures, such as multilayered samples or materials with thermal conductivity profiles extending into deeper regions, require additional databases to accurately model their thermal properties.

IV. CONCLUSION

Neural networks were integrated into the FDTR measurement system to develop a machine learning model capable of predicting thermal conductivity at various depths without predefined constraints on the functional form of the thermal conductivity profile. The implementation of the Monte Carlo dropout technique within the neural network architecture facilitated an enhanced analysis of prediction uncertainty. This methodology confirmed the model's ability to accurately analyze the thermal conductivity profile along the depth and compute prediction uncertainties that are typically challenging to ascertain theoretically. An analysis of average prediction uncertainty relative to depth within the test set revealed a notable increase in the prediction uncertainty near the surface and in deeper regions of the sample. These insights are instrumental in advancing the understanding of heat conduction phenomena in depth-specific thermophysical property measurements and in developing future analyses of multilayered structures using FDTR. Moreover, this method may be applicable to other thermophysical measurement techniques that manipulate thermal penetration

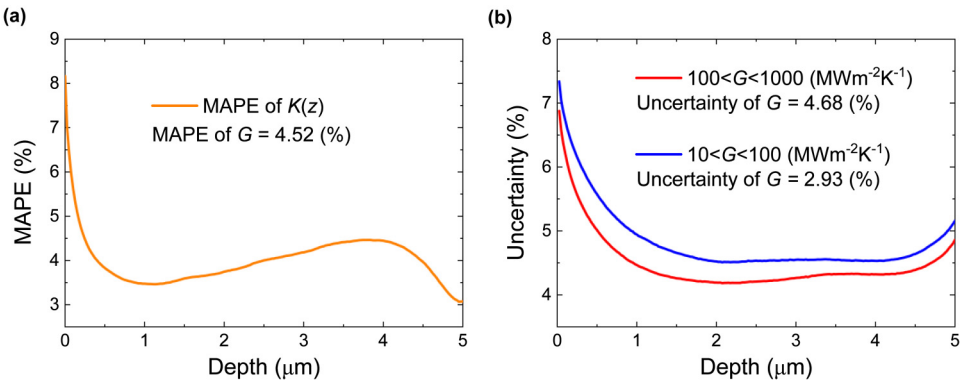

FIG. 5. (a) Evaluation of predictions for test sets by the machine learning model. The plots show the mean absolute percentage error (MAPE) in thermal conductivity $K(z)$ at various depths. (b) Prediction uncertainty for test sets by the machine learning model. The plots display prediction uncertainty in thermal conductivity across different depths. The blue (upper) and red (lower) curves represent low and high values of thermal boundary conductance G, respectively.

depth through periodic heating, such as the 3ω method, suggesting broader applications in future research efforts.

SUPPLEMENTARY MATERIAL

See the supplementary material for detailed information about our machine learning methodology and results.

ACKNOWLEDGMENTS

This work received financial support from JST PRESTO (JPMJPR20B6) and multiple JSPS Grants-in-Aid for Scientific Research (Nos. 19H02168, 20KK0087, 23K04361, and 23K26139). Computational resources were provided by the supercomputer at the ACCMS, Kyoto University.

AUTHOR DECLARATIONS

Conflict of Interest

The authors have no conflicts to disclose.

Author Contributions

Yasuaki Ikeda: Conceptualization (lead); Data curation (lead); Formal analysis (lead); Methodology (lead); Resources (lead); Software (lead); Visualization (lead); Writing – original draft (lead). **Yuki Akura:** Conceptualization (supporting); Formal analysis (supporting); Methodology (supporting); Resources (equal); Software (supporting); Writing – review & editing (equal). **Masaki Shimofuri:** Conceptualization (supporting); Writing – review & editing (supporting). **Amit Banerjee:** Conceptualization (supporting); Writing – review & editing (supporting). **Toshiyuki Tsuchiya:** Conceptualization (supporting); Project administration (lead); Writing – review & editing (supporting). **Jun Hirotani:** Conceptualization (lead); Funding acquisition (lead); Methodology (lead); Supervision (lead); Writing – review & editing (lead).

DATA AVAILABILITY

The data that support the findings of this study are available from the corresponding author upon reasonable request.

REFERENCES

[1]D. Etiemble, arXiv:1803.00254 (2018).
[2]J. Baek, Y. Elasser, K. Radhakrishnan, H. Gan, J. P. Douglas, H. K. Krishnamurthy, X. Li, S. Jiang, C. R. Sullivan, and M. Chen, IEEE Trans. Power Electron. **37**(6), 6305–6322 (2021).
[3]K. Chung, H. Oh, J. Jo, K. Lee, M. Kim, and G.-C. Yi, NPG Asia Mater. **9**(7), e410 (2017).
[4]A. Sood, J. Cho, K. D. Hobart, T. I. Feygelson, B. B. Pate, M. Asheghi, D. G. Cahill, and K. E. Goodson, J. Appl. Phys. **119**(17), 175103 (2016).
[5]Z. Cheng, T. Bougher, T. Bai, S. Y. Wang, C. Li, L. Yates, B. M. Foley, M. Goorsky, B. A. Cola, F. Faili, and S. Graham, ACS Appl. Mater. Interfaces **10**(5), 4808–4815 (2018).
[6]E. Chason, S. T. Picraux, J. M. Poate, J. O. Borland, M. I. Current, T. Diaz de la Rubia, D. J. Eaglesham, O. W. Holland, M. E. Law, C. W. Magee, J. W. Mayer, J. Melngailis, and A. F. Tasch, J. Appl. Phys. **81**(10), 6513–6561 (1997).
[7]E. López-Honorato, C. Chiritescu, P. Xiao, D. G. Cahill, G. Marsh, and T. J. Abram, J. Nucl. Mater. **378**(1), 35–39 (2008).
[8]C. Wei, X. Zheng, D. G. Cahill, and J.-C. Zhao, Rev. Sci. Instrum. **84**(7), 071301 (2013).
[9]K. Kim, W. Jeong, W. Lee, and P. Reddy, ACS Nano **6**(5), 4248–4257 (2012).
[10]Y. Zhang, W. Zhu, F. Hui, M. Lanza, T. Borca-Tasciuc, and M. Muñoz Rojo, Adv. Funct. Mater. **30**(18), 1900892 (2020).
[11]O. Braun, R. Furrer, P. Butti, K. Thodkar, I. Shorubalko, I. Zardo, M. Calame, and M. L. Perrin, npj 2D Mater. Appl. **6**(1), 6 (2022).
[12]J. Anaya, S. Rossi, M. Alomari, E. Kohn, L. Tóth, B. Pécz, and M. Kuball, Appl. Phys. Lett. **106**(22), 223101 (2015).
[13]A. Alasli, R. Fujita, and H. Nagano, Int. J. Thermophys. **43**(12), 176 (2022).
[14]D. G. Cahill, Rev. Sci. Instrum. **75**(12), 5119–5122 (2004).
[15]A. J. Schmidt, X. Chen, and G. Chen, Rev. Sci. Instrum. **79**(11), 114902 (2008).
[16]S. Huxtable, D. G. Cahill, V. Fauconnier, J. O. White, and J.-C. Zhao, Nat. Mater. **3**(5), 298–301 (2004).
[17]W. S. Capinski and H. J. Maris, Rev. Sci. Instrum. **67**(8), 2720–2726 (1996).
[18]L. Yates, A. Sood, Z. Cheng, T. Bougher, K. Malcolm, J. Cho, M. Asheghi, K. Goodson, M. Goorsky, F. Faili, D. J. Twitchen, and S. Graham, "Characterization of the thermal conductivity of CVD diamond for GaN-on-diamond devices," in *IEEE Compound Semiconductor Integrated Circuit Symposium CSICS* (IEEE, 2016), pp. 1–4.
[19]A. J. Schmidt, R. Cheaito, and M. Chiesa, Rev. Sci. Instrum. **80**(9), 094901 (2009).
[20]J. A. Malen, K. Baheti, T. Tong, Y. Zhao, J. A. Hudgings, and A. Majumdar, J. Heat Transf. **133**(8), 081601 (2011).
[21]K. T. Regner, D. P. Sellan, Z. Su, C. H. Amon, A. J. H. McGaughey, and J. A. Malen, Nat. Commun. **4**, 1640 (2013).
[22]X. Wang, M. Jeong, A. J. H. McGaughey, and J. A. Malen, Rev. Sci. Instrum. **93**(2), 023001 (2022).
[23]K. T. Regner, S. Majumdar, and J. A. Malen, Rev. Sci. Instrum. **84**(6), 064901 (2013).
[24]J. Liu, J. Zhu, M. Tian, X. Gu, A. Schmidt, and R. Yang, Rev. Sci. Instrum. **84**(3), 034902 (2013).
[25]A. J. Schmidt, R. Cheaito, and M. Chiesa, J. Appl. Phys. **107**(2), 024908 (2010).
[26]Y. Song, C. Perez, G. Esteves, J. S. Lundh, C. B. Saltonstall, T. E. Beechem, J. I. Yang, K. Ferri, J. E. Brown, Z. Tang, J.-P. Maria, D. W. Snyder, R. H. I. Olsson, B. A. Griffin, S. E. Trolier-McKinstry, B. M. Foley, and S. Choi, ACS Appl. Mater. Interfaces **13**(16), 19031–19041 (2021).
[27]N. Poopakdee, Z. Abdallah, J. W. Pomeroy, and M. Kuball, ACS Appl. Electron. Mater. **4**(4), 1558–1566 (2022).
[28]Z. Hua, H. Ban, M. Khafizov, R. Schley, R. Kennedy, and D. H. Hurley, J. Appl. Phys. **111**(10), 103505 (2012).
[29]H. Ma, Z. Hua, A. Sen, T. Yao, M. S. Bryan, A. Alatas, E. K. Nosal, S. Adnan, E. Xiao, A. French, M. Bachhav, C. A. Marianetti, M. Khafizov, L. Shao, L. He, J. P. Wharry, D. H. Hurley, and M. E. Manley, Phys. Rev. B **108**(10), 104318 (2023).
[30]T. W. Pfeifer, J. A. Tomko, E. Hoglund, E. A. Scott, K. Hattar, K. Huynh, M. Liao, M. Goorsky, and P. E. Hopkins, J. Appl. Phys. **132**(7), 075112 (2022).
[31]D. J. Kirsch, J. Martin, R. Warzoha, M. McLean, D. Windover, and I. Takeuchi, Rev. Sci. Instrum. **95**(10), 103006 (2024).
[32]C. Yuan, R. Hanus, and S. Graham, J. Appl. Phys. **132**(22), 220701 (2022).
[33]Y. Akura, Y. Ikeda, Y. Matsunaga, M. Shimofuri, A. Banerjee, T. Tsuchiya, and J. Hirotani, Rev. Sci. Instrum. **96**(1), 014902 (2025).
[34]W. Shen, D. Vaca, and S. Kumar, Nanoscale Microscale Thermophys. Eng. **24**(4), 138–149 (2020).
[35]Y. Pang, P. Jiang, and R. Yang, J. Appl. Phys. **130**(8), 084901 (2021).

[36]Z. Xiang, Y. Pang, X. Qian, and R. Yang, Appl. Phys. Lett. **122**(14), 142201 (2023).
[37]D. Svozil, V. Kvasnicka, and J. Pospichal, Chemom. Intell. Lab. Syst. **39**(1), 43–62 (1997).
[38]N. Srivastava, G. Hinton, A. Krizhevsky, I. Sutskever, and R. Salakhutdinov, J. Mach. Learn. Res. **15**(56), 1929 (2014).
[39]Y. Gal and Z. Ghahramani, arXiv:1506.02142 (2016).
[40]D.-A. Clevert, T. Unterthiner, and S. Hochreiter, arXiv:1511.07289 (2016).
[41]S. Hochreiter, Int. J. Uncertainty, Fuzziness Knowl.-Based Syst. **6**(2), 107–116 (1998).
[42]B. Hanin, arXiv:1801.03744 (2018).
[43]L. Lu, Y. Shin, Y. Su, and G. E. Karniadakis, Commun. Comput. Phys. **28**(5), 1671–1706 (2020).